Published in final edited form as:
Structure. 2020 September 01; 28(9): 1014–1023.e4. doi:10.1016/j.str.2020.06.002.

Crystal Structure of β-Arrestin 2 in Complex with CXCR7 Phosphopeptide

Kyungjin Min[#1], **Hye-Jin Yoon**[#1], **Ji Young Park**[2], **Mithu Baidya**[3], **Hemlata Dwivedi-Agnihotri**[3], **Jagannath Maharana**[3], **Madhu Chaturvedi**[3], **Ka Young Chung**[2,*], **Arun K. Shukla**[3,*], **Hyung Ho Lee**[1,5,*]

[1]Department of Chemistry, College of Natural Sciences, Seoul National University, Seoul 08826, Republic of Korea

[2]School of Pharmacy, Sungkyunkwan University, Suwon 16419, Republic of Korea

[3]Biological Sciences and Bioengineering, Indian Institute of Technology, Kanpur 208016, India

[#] These authors contributed equally to this work.

Summary

β-arrestins (βarrs) critically regulate G-protein-coupled receptor (GPCR) signaling and trafficking. βarrs have two isoforms, βarr1 and βarr2. Receptor phosphorylation is a key determinant for the binding of βarrs, and understanding the intricate details of receptor-βarr interaction is the next frontier in GPCR structural biology. The high-resolution structure of active βarr1 in complex with a phosphopeptide derived from GPCR has been revealed, but that of βarr2 remains elusive. Here, we present a 2.3-Å crystal structure of βarr2 in complex with a phosphopeptide (C7pp) derived from the carboxyl terminus of CXCR7. The structural analysis of C7pp-bound βarr2 reveals key differences from the previously determined active conformation of βarr1. One of the key differences is that C7pp-bound βarr2 shows a relatively small inter-domain rotation. Antibody-fragment-based conformational sensor and hydrogen/deuterium exchange experiments further corroborated the structural features of βarr2 and suggested that βarr2 adopts a range of inter-domain rotations.

[*]Correspondence: kychung2@skku.edu (K.Y.C.), arshukla@iitk.ac.in (A.K.S.), hyungholee@snu.ac.kr (H.H.L.).
[5]Lead Contact

Supplemental Information
Supplemental Information can be found online at https://doi.org/10.1016/j.str.2020.06.002.

Author Contributions
K.M. and H.-J.Y. resolved the crystal structure. M.B. carried out the confocal microscopy experiments and assisted in the Tango assay performed by H.D.-A. and M.C. H.D.-A. and J.M. measured the reactivity of Fab30 with C7pp-bound βarr2 using co-immunoprecipitation and ELISA. A.K.S. supervised the experiments performed by M.B., H.D.-A., J.M., and M.C. and contributed to the writing and editing of the manuscript. J.Y.P. generated the βarr2 constructs and performed HDX-MS. K.Y.C. supervised the experiments performed by J.Y.P. and contributed to the writing and editing of the manuscript. K.M., H.-J.Y., K.Y.C., A.K.S., and H.H.L. analyzed the data and wrote the manuscript. H.H.L. directed the teams. All authors edited the manuscript.

Declaration of Interests
The authors declare no competing interests

Europe PMC Funders Author Manuscripts

Europe PMC Funders Author Manuscripts

Introduction

G-protein-coupled receptors (GPCRs), also known as 7-transmembrane receptors (7TMs), are the largest family of receptors expressed on cell membranes and comprise an important class of drug targets. In response to ligand binding, GPCRs, which are guanine nucleotide exchange factors, activate G proteins, which then trigger downstream signaling. To turn off the G-protein-mediated GPCR signaling, GPCR kinases phosphorylate the C-terminal tail and/or the intracellular loops of GPCRs, which leads to arrestin binding. Although there are over 800 GPCRs in the human genome, only four arrestin genes (arrestins 1–4) have been identified. Among the four arrestin subtypes, arrestin-1 and arrestin-4 are solely related to rhodopsin and cone opsin in the visual system, whereas arrestin-2 and arrestin-3 (β-arrestin 1 and β-arrestin 2, hereafter βarr1 and βarr2, respectively) are ubiquitously expressed; they are responsible for interactions with and the regulation of nonvisual GPCRs. The interaction of βarrs with phosphorylated receptors transits βarrs to their active state, which leads to desensitization and/or internalization of GPCRs. It is also well established that βarrs critically contribute to a range of downstream signaling responses in many different GPCRs (DeWire et al., 2007). In addition, βarrs are also recognized as multifunctional and versatile adaptor proteins that bind to and regulate dozens of nonreceptor proteins (Lefkowitz et al., 2006). It is also worth noting that βarr2 has been shown to be more flexible than βarr1 (Sensoy et al., 2016; Zhan et al., 2011).

The binding of GPCRs and βarrs typically consists of two kinds of interactions, namely, docking of the phosphorylated (or unphosphorylated) receptor tail (i.e., the carboxyl terminus) to the N domain of βarrs and interaction of the receptor core (i.e., the intracellular side of the receptor transmembrane bundle) with the loops on the convex side of βarrs, although the actual sequence of the events remains unknown (Cahill et al., 2017; Celver et al., 2002; Gimenez et al., 2012; Gurevich and Gurevich, 2004; Kovoor et al., 1999; Shukla et al., 2014; Thomsen et al., 2016). While the primary cellular functions of βarrs are broadly conserved across different GPCRs, there is increasing evidence for receptor-specific fine-tuning of βarr functions. Although a clear mechanism for functional diversity of βarrs remains mostly elusive, it has been proposed that different patterns of receptor phosphorylation establish distinct phospho-clusters on the receptor that fine-tune the interaction pattern and conformational signatures of βarrs, resulting in specific functions (Mayer et al., 2019; Nobles et al., 2011; Reiter and Lefkowitz, 2006; Xiao et al., 2007; Yang et al., 2015). To decode how distinct phosphorylation patterns govern the conformations and functional outputs of βarrs, it is essential to visualize the structural details of βarrs in complex with differentially phosphorylated GPCRs or their corresponding phosphopeptides.

There has been significant effort in recent years to understand the molecular mechanism of βarr activation, including studies of crystal structures of preactivated arrestin-1 (Kim et al., 2013), βarr1 in complex with the phosphorylated vasopressin receptor tail (V_2Rpp) (Shukla et al., 2013), and rhodopsin-arrestin-1 fusion protein (Kang et al., 2015; Zhou et al., 2017). These structures have revealed major conformational changes that occur upon arrestin-1 and βarr1 activation, such as significant inter-domain rotation (~20°), disruption of three-element (3E) and polar-core interactions, and reorientation of various loops, including the finger and lariat loops (Hirsch et al., 1999). The study of structure of V_2Rpp-bound βarr1 also

confirmed a previously suggested molecular mechanism, in which the binding of the phosphorylated receptor tail to the N domain of an arrestin displaces the carboxyl terminus of the arrestin (Palczewski et al., 1991; Xiao et al., 2004). Furthermore, in addition to a phosphorylation-dependent interaction, the crystal structure of rhodopsin-arrestin-1 fusion protein has also provided the structural details of a fully engaged complex, including the interface between arrestin-1 and the receptor core (Kang et al., 2015; Zhou et al., 2017). The crystal structures of inositol hexakisphosphate (IP_6)-activated βarr2, C-terminal truncated p44, and R175E mutant visual arrestin 1 also exhibited their active conformations (Cahill et al., 2017; Granzin et al., 2015; Kim et al., 2013). Single-particle negative-staining-based electron microscopy has facilitated direct visualization of the biphasic interaction between the receptor and βarr1 by capturing the partially engaged (associated through the receptor tail) and fully engaged (involving the receptor core) complexes (Shukla et al., 2014). Recently, the structure of βarr1 in complex with neurotensin receptor 1 showed an overall assembly that is strikingly different from that of the visual arrestin-rhodopsin complex (Yin et al., 2019).

However, the activation of βarr2 by a phosphorylated receptor and difference between the activation of βarr2 and βarr1 or visual arr1 remain to be structurally visualized. This is particularly important considering that despite ubiquitous expression and high sequence similarity, βarr1 and βarr2 display a significant level of functional divergence (DeWire et al., 2007; Srivastava et al., 2015). For example, some GPCRs bind βarr2 with higher affinity than βarr1 while others bind both the isoforms with similar affinities (Oakley et al., 2000). Moreover, in some cases, the two isoforms of βarrs contribute differentially toward their conserved functions of receptor desensitization, endocytosis, and signaling (Srivastava et al., 2015). Additionally, for some receptors such as the bradykinin and angiotensin receptors, depletion of βarr2 results in decreased agonist-induced ERK1/2 MAP kinase phosphorylation, while depletion of βarr1 enhances the phosphorylation (Wei et al., 2003; Zimmerman et al., 2011). Thus, to fully understand βarr-mediated regulation of GPCRs and to delineate the functional divergence among βarrs, visualization of the structural details of activation of βarr2 by a phosphorylated receptor tail is essential.

Accordingly, in this study we focused on capturing the active conformations of βarr2 in complex with phosphopeptides originating from the carboxyl terminus of the chemokine receptor CXCR7, also referred to as atypical chemokine receptor 3 (ACKR3). CXCR7, a class A GPCR, forms a heterodimer with another chemokine receptor, CXCR4. It has been proposed that CXCR7 acts as a “scavenger” of CXCL12, a chemokine ligand of CXCR4 (Rajagopal et al., 2010). It has also been suggested that CXCR7 may represent a natural example of a βarr-biased 7TM receptor, as it interacts with βarrs but does not display functional coupling with heterotrimeric G proteins (Rajagopal et al., 2010). Here, we determine the crystal structure of βarr2 in complex with a CXCR7 phosphopeptide. The structure revealed key differences from the previously determined structures of arrestins including V_2Rpp-bound βarr1. In addition, we utilized a diverse set of complementary biochemical and biophysical approaches, including site-directed mutagenesis, hydrogen/deuterium exchange mass spectrometry (HDX-MS), and synthetic-antibody-based conformational sensors, to acquire insights into the activation of βarr2.

Results and Discussion

Agonist-Induced β-arrestin Recruitment and Trafficking by CXCR7

CXCR7 does not exhibit functional coupling with any of the major subtypes of heterotrimeric G proteins, although it does efficiently couple to βarr2 (Rajagopal et al., 2010). We first validated βarr2 coupling and trafficking in HEK-293 cells using a PRESTO-TANGO assay (Kroeze et al., 2015) and confocal microscopy (Figures 1A and 1B). We observed that CXCR7 efficiently recruits βarr2 and behaves as a class B receptor in terms of its pattern of trafficking βarr2 (i.e., receptors are internalized). Based on a recent study that proposed the importance of different phosphorylation codes in GPCRs for βarr binding (Zhou et al., 2017), we searched a crystallizable phosphorylation code in the carboxyl terminus of CXCR7 (Figure S1A). It should be noted that previous studies have reported the functional significance of the carboxyl terminus of CXCR7 (Hoffmann et al., 2012; Saaber et al., 2019).

Generation and Characterization of CXCR7 Phosphopeptides

We synthesized a phosphopeptide to investigate its interaction with βarr2 and any corresponding structural changes (Figure 1C). The peptide harbored the PxxPxxP pattern of phosphorylation, referred as to C7pp (Figures 1C and S1A), and was used to acquire an insight into the phospho-cluster-dependent structural changes of βarr2. The C7pp exhibited a binding affinity to *rat* βarr2, with dissociation constant (K_D) of 3.08 ± 0.3 μM as measured by isothermal titration calorimetry, displaying a monophasic binding with βarr2 (Figure 1D).

To understand the structural changes of βarr2 upon C7pp binding, we performed HDX-MS (Figure 1E). HDX-MS monitors the exchange between the amide hydrogen of a protein and deuterium in the solvent, and the exchange rate is dependent on the conformational flexibility and/or solvent exposure of the amide hydrogen (Konermann et al., 2011; Skinner et al., 2012; Wales and Engen, 2006). The HDX-MS profiles of βarr2 with or without co-incubation of C7pp were analyzed, which showed that C7pp binding induced iconic changes in active arrestins. We observed increased HDX within residues 383–390 containing βXX and residues 292–301 containing the gate loop (the C-terminal part of the lariat loop), which implied release of the C terminus and disruption of the polar core. Additionally, we observed decreased HDX within residues 119–133 containing the middle loop, residues 283–291 containing the N-terminal part of the lariat loop, and residues 305–317 containing the back loop, which implied the possible movement of the inter-domain regions (Shukla et al., 2013).

Crystal Structure of Phosphopeptide-Bound βarr2

To reveal the atomic details of C7pp-bound βarr2, we performed X-ray crystallography to obtain high-resolution structures. Although C7pp binds efficiently to full-length βarr2 (Figures 1D and 1E), we used a truncated version of βarr2 that lacked the carboxyl-terminal residues 357–410 to facilitate crystallization of βarr2 in an active conformation, while all other biochemical experiments were performed using full-length βarr2. Caution was warranted while using the truncated version of βarr2 because the truncation may shift the equilibrium of βarr2 to active conformation. However, C7pp bound to the full-length βarr2

in solution (Figure 1D) and induced increased HDX at βXX (Figure 1E), suggesting that C7pp can release βXX from the N domain of βarr2. Moreover, the HDX profile of truncated βarr2 did not change upon co-incubation with C7pp (data not shown). Thus, we concluded that the C-terminal truncated version of βarr2 in complex with C7pp could represent the active conformation of βarr2 induced by C7pp binding.

We obtained a 2.3-Å crystal structure of βarr2 in complex with C7pp (Figures 2A and S2) and focused our discussion on the conformational details of C7pp-bound βarr2.

The crystals of C7pp-bound βarr2 appeared to be pseudo-merohedrally twinned in the $C2_1$ space group with a high R_{merge} value; thus, the structure was refined with detwinned data (Table 1). The electron density map of residues 331–332 of C7pp (chain U) was not observed, while nearly all sequences of βarr2 were found to be ordered with the exception of the internal flexible regions (residues 175–181 in chains C and F, respectively) (Figure S2). C7pp adopted an elongated loop over the entire length (~35 Å) without severe kinking and was paired with the highly cationic concave surface of the N domain of βarr2, with a total surface area of 928.4 $Å^2$ buried at the interface (Figure S3).

While interpreting the structural changes in βarr2 upon C7pp binding, especially in terms of comparing them with other X-ray crystal structures of arrestins, caution was warranted during analysis of the regions involved in crystal contacts, as it may sometimes lead to crystallographic artifacts. Interestingly, the crystallographic asymmetric unit of the βarr2-C7pp complex consisted of six heterodimers of βarr2 and C7pp and revealed that the crystallographic contacts of the six molecules are not identical to each other (Figure S2A). Thus, we were able to find at least one solvent-exposed region among the six molecules for activation-dependent regions, which allowed us to confidently interpret the C7pp-induced structural changes in βarr2. Moreover, the six βarr2-C7pp molecules showed essentially similar structures overall when they were superimposed (average root-mean-square deviation [RMSD] of 1.14 Å for the 334 Cα atom pairs) (Figure S2B).

Smaller Inter-domain Rotation in C7pp-βarr2 Compared with that in V_2Rpp-βarr1

The structure of C7pp-bound βarr2 exhibited conformational changes similar to those in other existing active arrestin structures (βarr1, βarr2, or visual arr1), such as disruption of the 3E interaction and polar-core interaction (discussed in Figures 3 and S5). However, the most striking difference between C7pp-bound βarr2 and V_2Rpp-bound βarr1 was found in the inter-domain rotation angle (Figures 2C, 2D, and S4). The inter-domain rotation angle of C7pp-bound βarr2 was found to be significantly smaller (~8°) than that of V_2Rpp-bound βarr1 (~20°) (PDB: 4JQI) (Figure 2D). The smaller inter-domain rotation is observed in visual arr1 when Arg175 is mutated to Glu in the absence of a phosphopeptide (PDB: 4ZRG) and in C-terminal truncated visual arr1 (PDB: 3UGU) (Granzin et al., 2012, 2015). Conversely, a larger inter-domain rotation (18°–20°) is observed in other arrestin structures (PDB: 4J2Q, 5TV1, 4ZWJ, and 5W0P) (Cahill et al., 2017; Kang et al., 2015; Kim et al., 2013; Zhou et al., 2017). It is interesting to note that receptor-mediated activation of βarr1 (PDB: 4JQI) and visual arr1 (PDB: 4ZWJ and 5W0P) induces the larger inter-domain rotation, while in our study C7pp-bound βarr2 adopted smaller inter-domain rotation. These data led us to propose two hypotheses: first, unlike the receptor-bound βarr1 or visual arr1,

the receptor-bound βarr2 adopts a structure with smaller inter-domain rotation when it interacts with a phosphorylated receptor C-tail; and second, βarr2 adopts structures with various inter-domain rotations depending on the binding partners.

To test the first hypothesis, we measured the reactivity of a conformationally selective antibody fragment, Fab30, toward C7pp- and V_2Rpp-bound βarr2. Fab30 efficiently interacts with V_2Rpp-bound βarr1 and βarr2, and molecular dynamics simulations have suggested that an inter-domain rotation of more than 15° is most optimal for Fab30 reactivity (Ghosh et al., 2019). We did not observe a significant interaction of Fab30 with C7pp-bound βarr2 (Figures 2E and 2F). This was consistent with the smaller inter-domain rotation observed in the C7pp-bound crystal structure of βarr2 (Figure 2C). However, Fab30 interacted robustly with V_2Rpp-bound βarr2 (Figures 2E and 2F). These results suggested that βarr2 adopts different conformations when bound to different R_p-tails or different activation stimuli and thus led to rejection of the first hypothesis—the smaller inter-domain rotation in C7pp-bound βarr2 structure may indicate an inherent propensity specific to βarr2 upon its activation.

An alternative hypothesis is that specific phosphorylation patterns, i.e., the number and spatial distribution of phosphates, govern the inter-domain rotation and thereby impart the corresponding functional conformation to βarr2. Although such a possibility remains to be explored further, it may explain not only the structural basis of the barcode hypothesis but also the receptor-specific functional outcomes of βarrs. Therefore, we suggest that the current C7pp-bound βarr2 structure represents one of the active conformations that may be observed for other receptors as well, depending on the specific phosphorylation pattern. It is also tempting to suggest that this applies to βarr1 and visual arr1 as well, depending on cellular and functional context. Considering that even partially engaged receptor-βarr conformations are functionally competent, for example, in terms of mediating receptor endocytosis and ERK1/2 MAP kinase activation (Cahill et al., 2017; Kumari et al., 2016), the current structure has direct implications for understanding the structural details of receptor-βarr interaction and for ensuring functional responses. It should also be noted that the structure represents the conformation of βarr2 in complex with an isolated phosphopeptide without including the receptor core interaction. It is also plausible that the core interaction may further fine-tune the conformation of βarr2, including the inter-domain rotation angle. Collectively, these data support the previously proposed model that βarr2 adopts a range of inter-domain rotations, with the domain rotation aligning the different parts of βarr2 to create a potential effector-binding site, resulting in various functional outcomes (Chen et al., 2018).

Distinct Conformational Changes of the Loop Regions in the C7pp-βarr2 Structure

To gain further structural insights into the conformation of βarr2 induced upon its binding to C7pp, we compared our structure of C7pp-bound βarr2 with two groups of arrestin structures, one group with smaller inter-domain rotation (group 1 in Figure 2D) and the other group with larger inter-domain rotation (group 2 in Figure 2D). The two active molecules of visual arr1 with smaller inter-domain rotation show essentially similar structures; hence, we used visual arr1 R175E structure (PDB: 4ZRG) for comparison with

the structure of C7pp-bound βarr2. Among the arrestin structures with larger inter-domain rotation, V_2Rpp-bound βarr1 (PDB: 4JQI) was mainly used to determine the effect of the phosphopeptide, and IP_6-bound βarr2 (PDB: 5TV1) was used to determine the different active statuses of βarr2. All of these active structures exhibited disruption of 3E and polar-core interactions (examples are illustrated in Figures 3D and S5).

As discussed above, the N domain and central loops showed large conformational changes upon activation (Scheerer and Sommer, 2017). Despite the intrinsic flexibility of each loop containing the central crest, the conformations of the six βarr2-C7pp molecules in the asymmetric unit matched exceedingly well with each other (Figure S2B), suggesting that none of the conformations was derived from a crystallographic artifact but were the consequence of activation of βarr2 upon its binding to C7pp.

The loop regions underwent conformational changes upon C7pp binding, and the structures were different in several ways from those of other active state arrestin structures (Figures 3A–3C). First, the C7pp peptide occluded the inactive conformation of the finger loop lock, promoted outward movement, and induced a helical structure in our crystal structure (Figures 3A and 3B, left panel, blue). This was surprising because the finger loop of the βarr1-V_2Rpp complex exhibited an extended conformation (Shukla et al., 2013) (Figure 3C, left panel, light cyan), and the helical structure of the finger loop was often observed when the arrestin was fully docked to the GPCR core. However, it should be noted that HDX-MS analysis did not indicate a helix formation in the finger loop (Figure 1E), suggesting that the helix observed in the current structure might be short-lived and in a transient state. It is also worth noting that IP_6-bound βarr2 showed helix formation in the finger loop (Figure 3C, left panel, light blue). Second, the middle loop structure was different and did not overlap with the structures of other arrestins (Figures 3A and 3B, middle panel). Third, the lariat loop moved most closely to the N domain and formed van der Waals interactions with C7pp (Figures 3A and 3B, right panel). Lys296 (the corresponding residue of Lys294 in βarr1), belonging to the lariat loop, moved toward C7pp, which might have provided an additional driving force for lariat loop arrangement (Figures 3A and 3B, right panel). A similar movement was observed in the IP_6-bound βarr2 (Figure 3C, right panel). Based on these observations, we propose that the inter-domain rotation angle does not determine the structure of the three loops (finger, middle, and lariat loops). Given that these loops were distributed across the surface of βarr2, different phosphorylation patterns of the GPCR R_p-tail might induce distinct conformations of βarr2 in a combinatorial manner. Conversely, the C loop, which was crucial in interacting with GPCR core, exhibited different positions depending on the inter-domain rotation angle (Figures 3A and 3B, left panel). The arrestin structures with smaller inter-domain rotation resided in similar positions but not in the same position (Figures 3A and 3B). Collectively, our structure does not exactly overlap with previously determined structures of arrestins, reflecting the high flexibility of arrestins.

Distinct Binding Modes of C7pp Compared with Other R_p-Tails

After the examination of the conformations of six C7pp peptides in a crystallographic asymmetric unit, two types of conformations (chain U versus chains V/W/X/Y/Z) were observed with slightly different modes of βarr2 recognition (Figure S2C). Therefore, there

could be an ensemble of multiple conformations of C7pp when it interacts with positively charged residues distributed on the surface of βarr2 (Figure S3). Given that the N domain of βarr2 should interact with hundreds of different patterns of the GPCR R_p-tail, the complex between them might be modular, which has often been observed in disordered proteins (Miskei et al., 2017; Sente et al., 2018). The large dependence of electrostatic interactions between βarr2 and R_p-tails might allow βarr2 to pair with hundreds of GPCRs containing different phosphorylated R_p-tails.

To investigate the manner in which the binding mode of C7pp was distinct from those of V_2Rpp and the rhodopsin C-tail, we compared the conformations of these different structures (Figures 4A, 4B, S3B, and S3D). For the structural comparisons, we chose the C7pp (chain U) bound to βarr2 with chain A. It has been shown previously that the phosphopeptides overlap reasonably well when the structure of the rhodopsin-arrestin complex is superimposed with that of the βarr1-V_2Rpp complex (Zhou et al., 2017). However, when we superimposed the βarr2-C7pp complex with the βarr1-V_2Rpp complex, the overall conformations of C7pp and V_2Rpp were significantly different (Figure 4A). The N-terminal part of C7pp was closer to the β7/β8 loop than that of the V_2Rpp, whereas the C-terminal part of C7pp was shorter (Figure 4A). The N- and C-terminal parts of the V_2Rpp made a continuous β sheet with β4 and β1, respectively, of βarr1 by anti-parallel stacking, especially in βarr1. However, those parts of C7pp did not interact directly with either β4 or β1 of βarr2 (Figure 4A).

Interaction of Phosphopeptide with βarr2

Detailed examination of the phosphate-binding sites provided us with further insight into the different binding modes of C7pp compared with other R_p-tails. C7pp contains three phosphates, which consist of the very frequently observed phosphorylation pattern (PxxPxxP) in the GPCR C terminus. Three positively charged pockets (pocket A, pocket B, and pocket C) might recognize the phosphorylated serine or threonine consisting of the PxxPxxP pattern (Zhou et al., 2017). pSer357 and pThr360 (the first and second phosphates) of V2Rpp are nearly superimposable with pThr336 and pSer338 of the rhodopsin C-terminal tail, which bind to pocket A and pocket B, respectively (Zhou et al., 2017) (Figure S6A).

The three phosphates of C7pp make extensive contact with the positively charged residues on βarr2 (Figure 5). The first, second, and third phosphates (pSer335, pThr338, and pThr341) form a salt bridge with βarr2 Arg148 (2.3 Å) (box P), Arg166 (3.0 and 3.4 Å) (box A), and Arg26 (2.9 Å) (box B), respectively. Side chains of many other residues (Lys333, Lys337, Gly339, Lys342, Leu343, and Asp345), except for the phosphorylation sites (pSer335, pThr338, and pThr341), point in the opposite direction to the interface of βarr2 and C7pp (Figure 5); therefore, the side chains of other residues do not contribute markedly to βarr2 binding.

Instead of utilizing the same pockets (A, B, and C) in rhodopsin, the new pocket around Arg148 recognized the first phosphate (pSer335) (Figure 5, box P), whereas pockets A and B interacted with the second and third phosphates (pThr338 and pThr341, respectively) (Figure 5, boxes A and B). Therefore, the binding mode of PxxPxxP pattern was different in the βarr2-C7pp complex. We designated the newly identified pocket, which interacted with

the first phosphate (pSer335), as pocket P (Figure 5, box P). Next, we checked whether the three pockets (P, A, and B) could accommodate the binding of the PxPxxP pattern, for which they were responsible. It appeared that the space between the first and second phosphates could accommodate either one or two residues because the nearby Lys161 (Figure 5, box P), which is a strictly conserved residue (Figure 5), might interact with the first phosphate of the PxPxxP pattern. The phosphate sensor residues (Arg8, Lys10, Lys11, Lys107, and Lys294 in βarr1) that make contact with the V_2Rpp phosphates are not involved in the interactions with C7pp (Gurevich and Gurevich, 2004; Shukla et al., 2013) (Figures S1B and S6). The newly identified phosphate-binding pocket, pocket P, might be involved in the different conformational changes of C7pp-bound βarr2 (e.g., smaller inter-domain rotation and different loop structures) compared with the V_2Rpp-bound βarr1, which requires further investigation. Together, these data suggest that various GPCR R_p-tails with different phosphorylation patterns might bind to arrestins differently, which may provide not only the strength of the interaction but also the ensuing functional outcomes.

Concluding Remarks

One characteristic of ACKRs, including CXCR7, is their inability to functionally couple with G proteins while maintaining robust interaction with βarrs. Thus, it is tempting to speculate that the conformational differences observed here for C7pp-bound βarr2, compared with V_2Rpp-bound βarr1, may reflect a general feature of ACKRs. However, this possibility must be experimentally validated in the future for other ACKRs. There also exists a significant functional divergence between the two isoforms of β-arrestins, βarr1 and βarr2. Thus, it is plausible that the conformational differences between V_2Rpp-bound βarr1 and C7pp-bound βarr2 represent the mechanistic basis of this functional divergence. For example, βarrs have a direct contribution to agonist-induced ERK activation for V_2R, but for CXCR7, ERK1/2 activation was not observed (Rajagopal et al., 2010). Thus, the C7pp-bound βarr2 structure may represent one of the active conformations that are not competent for activating ERK1/2 but do support receptor endocytosis and, thus, ligand scavenging. However, this hypothesis requires additional experimentation in the future, including structure determination with a phosphorylated CXCR7.

In conclusion, we presented a C7pp-bound structure of βarr2 that exhibited key structural differences with the previously determined V_2Rpp-bound βarr1. These findings shed light on the functional divergence of the two βarr isoforms and underline the conformational flexibility in βarrs, which allows them to interact with multiple receptors and mediate distinct functional outcomes. Thus, our data provide useful information to obtain a better understanding of receptor-βarr interaction and signaling.

Supporting Citations

The following reference appears in the Supplemental Information: Laskowski and Swindells, 2011.

Star★Methods

Key Resources Table

REAGENT or RESOURCE	SOURCE	IDENTIFIER
Antibodies		
HRP-coupled Protein-L antibody	GenScript	Cat# M00098
Fab 30	This study	N/A
HRP-coupled M2 anti-FLAG antibody	Sigma-Aldrich	Cat# A8592; RRID: AB_439702
Bacterial and Virus Strains		
E. coli cells BL21(DE3)pLysS	Novogen	Cat# 71403
Chemicals, Peptides, and Recombinant Proteins		
Protein-L beads	GE Healthcare	Cat# 17547802
C7pp peptide	NovoPep	N/A
LB media	LPS solution	Cat# LB-005
Chloramphenicol	Bio Basic Inc.	Cat# 56757
Kanamycin	LPS solution	Cat# KAN025
M9 minimal salt media	Sigma-Aldrich	Cat# MKCF5138
IPTG	LPS solution	Cat# IPTG025
PMSF	Bio Basic Inc.	Cat# PB0425
Paratone® N oil	Sigma-Aldrich	Cat# HR2-643
n-dodecyl-β-D-maltopyranoside	Anatrace	Cat# D310S
Deposited Data		
Rat βarr2-C7pp complex structure	This study	6K3F
Bos Taurus βarr2	Zhan et al., 2011	3P2D
Bos Taurus βarr2	Chen et al., 2017	5TV1
Bovine βarr1	Milano et al., 2002	1JSY
Bos Taurus βarr1	Kang et al., 2009	3GC3
Rat βarr1	Shukla et al., 2013	4JQI
Bos Taurus βarr1	Han et al., 2001	1G4M
Ambystoma tigrinum visual arr1	Sutton et al., 2005	1SUJ
Bos Taurus visual arr1	Hirsch et al., 1999	1CF1
Bos Taurus visual arr1	Granzin et al., 2012	3UGX
Bos Taurus visual arr1	Granzin et al., 2012	3UGU
Bos Taurus visual arr1	Granzin et al., 2015	4ZRG
Bos Taurus visual arr1	Granzin et al., 1998	1AYR
Mouse visual arr1	Kang et al., 2015	4ZWJ
Mouse visual arr1	Zhou et al., 2017	5W0P
Squid visual arr1	Bandyopadhyay et al., 2018	6BK9
Experimental Models: Cell Lines		
HEK-293 cells	ATCC	Cat# CRL-3216
HTLA cells	Barnea et al., 2008	N/A

Europe PMC Funders Author Manuscripts

REAGENT or RESOURCE	SOURCE	IDENTIFIER
Recombinant DNA		
pET28a-βarr2$_{1-410}$	This study	N/A
pET28a-βarr2$_{1-356}$	This study	N/A
Software and Algorithms		
GraphPad Prism 6.0	GraphPad	graphpad.com
PyMol 1.8	Schrodinger LLC	pymol.org
Phaser	McCoy et al., 2007	phenix-online.org
COOT	Emsley and Cowtan, 2004	mrc-lmb.cam.ac.uk
REFMAC5	Murshudov et al., 1997	ccp4.ac.uk/html/refmac5.html
XDS	Kabsch, 2010	xds.mpimf-heidelberg.mpg.de
ProteinLynx Global Server (PLGS) 2.4	Waters	waters.com
DynamX 2.0	Waters	waters.com
Other		
Ni-sepharose affinity column	GE Healthcare	Cat# 17256801
Desalting column	GE Healthcare	Cat# 17085101
HiTrap Q sepharose column	GE Healthcare	Cat# 17115401
HiLoad 16/60 Superdex 200	GE Healthcare	Cat# 28989335
HiTrap heparin column	GE Healthcare	Cat# 17040701
96-well MaxiSorp polystyrene plates	Sigma-Aldrich	Cat# P6366

Resource Availability

Lead Contact—Further information and requests for resources and reagents should be directed to and will be fulfilled by the Lead Contact, Hyung Ho Lee (hyungholee@snu.ac.kr).

Materials Availability—All unique reagents generated in this study are available from the Lead Contact without restriction.

Data and Code Availability—The accession number for the βarr2-C7pp complex reported in this paper is Protein Data Bank ID: 6K3F

Experimental Model and Subject Details

Mammalian Cell Culture—HEK293 cells (Female) and HTLA cells (Female) were cultured in DMEM (SIGMA), 10% FBS (Thermo Fisher) and Penicillin-Streptomycin (100 U/ml penicillin + 100 μg/ml streptomycin) and maintained at 37°C under5% CO_2. The cells were sub-cultured at 70-80% confluency using 0.05% trypsin-EDTA (Thermo Fisher).

Bacterial Cell Culture—The *Rattus norvegicus* βarr2 plasmids were transformed into *Escherichia coli* BL21(DE3)pLysS cells (Invitrogen), and cells harboring the plasmids were grown at 37°C until the optical density (at 600 nm) reached 0.7–1.0 in Luria Bertani (LB)

broth or M9 minimal salt media (Sigma-Aldrich) containing 70 μg mL^{-1} chloramphenicol and 30 μg mL^{-1} kanamycin.

Method Details

Crystallization and Data Collection—Before crystallization, $\beta arr2_{1–356}$ (12 μg mL^{-1}) in buffer B containing 200 mM NaCl and C7pp peptide (70 mg mL^{-1}) in 150 mM Tris pH 8.0 were mixed in a 7:1 volume ratio and incubated at 4°C for 1 h. Crystals of the $\beta arr2_{1–356}$-C7pp complex were grown at 22°C using sitting-drop vapor diffusion by mixing 1 μL of the protein complex solution with 1 μL of 20% (w/v) PEG 3350, 0.2 M ammonium acetate, and 0.1 M Bis-tris pH 5.5. Crystals were cryoprotected by soaking in Paratone®N oil (Sigma-Aldrich) and flash frozen in liquid nitrogen. X-ray diffraction data were collected at 100 Kin 1° oscillations at the BL26B1 beamline of aSPring-8 (Japan). Raw data were processed and scaled using the XDS program suite (Kabsch, 2010). Table 1 summarizes the data collection statistics. The $\beta arr2_{1–356}$-C7pp complex crystal belonged to the space group $C2_1$, with unit cell parameters of $a = 91$ Å, $b = 127$ Å, and $c = 206$ Å (Table 1).

Structure Determination and Refinement—The structure of the $\beta arr2_{1–356}$-C7pp complex was solved by the molecular replacement method using a model of mouse visual arr1 (PDB code 5W0P). A cross-rotational search followed by a translational search was performed using the *Phaser* program (McCoy et al., 2007). Subsequent manual model building was performed using the *COOT* program (Emsley and Cowtan, 2004) and restrained refinement was performed using the *REFMAC5* program (Murshudov et al., 1997). Several rounds of model building, simulated annealing, positional refinement, and individual B-factor refinement were performed. Table 1 lists the refinement statistics. The asymmetric unit of the $\beta arr2_{1–356}$-C7pp complex contained six molecules of $\beta arr2_{1–356}$ and peptides, where chains A, B, C, D, E, and F corresponded to $\beta arr2_{1–356}$ and chains U, V, W, X, Y, and Z corresponded to the C7pp peptide. This model included 524 water molecules and 83.3% of the residues were in the most allowed region of the Ramachandran plot. No electron density was observed for residues 175–181 in chains C and F.

Cloning, Protein Expression, and Purification—CXCR7 phosphopeptide (C7pp) for crystallization, HDX-MS, and isothermal titration calorimetry (ITC) experiments were obtained from NovoPep (Figure 1C). The *R. norvegicus* wild-type $\beta arr2_{1–410}$ and C-terminal truncated $\beta arr2_{1–356}$ were inserted into expression vector pET28a. The plasmids were transformed into E. *coli* BL21(DE3)pLysS cells (Invitrogen), and cells harboring the plasmids were grown at 37°C until the optical density (at 600 nm) reached 0.7–1.0 in LB broth containing 70 μg mL^{-1} chloramphenicol and 30 μg mL^{-1} kanamycin. For the crystallization experiment, cells harboring $\beta arr2_{1–356}$ were grown at 37°C until the optical density (at 600 nm) reached 1.0 in M9 minimal salt media (Sigma-Aldrich) containing 70 μg mL^{-1} chloramphenicol and 30 μg mL^{-1} kanamycin. Further, 0.1 mM isopropyl-β-D-1-thiogalactopyranoside (IPTG) was used to induce protein expression in the cells, after which the cells were incubated for 16 h at 16°C. All constructs were verified by DNA sequencing.

For the isolation of the $\beta arr2_{1–356}$ protein fused to an N-terminal His_6 tag, cells were harvested by centrifugation at 5000 rpm at 4°C for 10 min and the pellet was resuspended in

Europe PMC Funders Author Manuscripts

ice-cold buffer A (20 mM Tris-HCl pH 8.0 and 500 mM NaCl) containing 1 mM phenylmethanesulfonylfluoride (PMSF). The cells were lysed using a microfluidizer (Microfluidics, Westwood, MA, USA) and the lysed cells were centrifuged at 15 000 rpm (Vision V506CA rotor) at 4°C for 30 min to separate the supernatant and cell debris. The supernatant was applied to a Ni-sepharose affinity column (GE Healthcare, Little Chalfont, UK) pre-equilibrated with buffer A. Initially, the column was washed extensively with buffer A, after which the protein was eluted using buffer A containing a gradient of imidazole concentrations from 100 mM to 1 M. The eluates were desalted into buffer B (20 mM Tris-HCl pH 8.0 and 5 mM β-mercaptoethanol) containing 100 mM NaCl using a desalting column (GE Healthcare) and further purified by anion-exchange chromatography with a HiTrap Q sepharose column (GE Healthcare). The proteins were eluted using buffer B containing 500 mM NaCl in a Q column. Further purification was performed by gel filtration on a HiLoad 16/60 Superdex 200 prep-grade column (GE Healthcare), which was equilibrated with buffer B containing 200 mM NaCl. For $\beta arr2_{1–410}$, the purification steps were the same as those for the $\beta arr2_{1–356}$ construct until the application to the desalting column (GE Healthcare). After desalting into buffer B, the protein was applied to a HiTrap heparin column (GE Healthcare) and eluted using buffer B containing 1 M NaCl. Further purification was performed by gel filtration on a HiLoad 16/60 Superdex 200 prep-grade column (GE Healthcare), which was equilibrated with buffer B containing 200 mM NaCl. The homogeneity of the purified protein was assessed by polyacrylamide gel electrophoresis in the presence of 0.1% (w/v) sodium dodecyl sulfate. The protein solution was concentrated to approximately 12 mg mL^{-1} using a Centricon centrifugal filter unit (Sartorius Stedim). The protein concentration was estimated by measuring the absorbance at 280 nm.

Isothermal Titration Calorimetry (ITC)—ITC experiments were performed using Affinity ITC instruments (TA Instruments, New Castle, DE, USA) at 298 K. A 100 μM sample of $\beta arr2_{1–410}$ WT, which was prepared in a buffer solution containing 20 mM Tris-HCl pH 8.0, and 200 mM NaCl was degassed at 295 K prior to the measurements being taken. Using a micro-syringe, 2.5 μL of 750 mM C7pp peptide solution was added at intervals of 200 s to the $\beta arr2_{1–410}$ WT solution in the cell with gentle stirring. A 30 μM sample of $\beta arr2_{1–410}$ WT was prepared in a buffer solution containing 20 mM Tris-HCl pH 8.0 and 200 mM NaCl was degassed at 295 K prior to the measurements being taken.

ELISA—For dose-response ELISA, the purified βarr2 was incubated with 10-fold molar excess V_2Rpp and C7pp for 30 min. Then, varying concentrations of peptide bound or unbound βarr2 was immobilized in 96-well MaxiSorp polystyrene plates (Nunc) at 298 K for 1 h. The potential non-specific binding sites in the wells were then blocked by incubation with 1% BSA at room temperature for 1 h. Subsequently, purified Fab 30 (1 μg/100 μL/well) was added to the wells and incubated at room temperature for 1 h. Wells were washed extensively using 20 mM Hepes pH 7.4, 150 mM NaCl, and 0.01% MNG and then incubated in a 1:2000 dilution of HRP-coupled Protein-L antibody (GenScript). After 1 h of incubation, the wells were thoroughly washed and the entire residual buffer removed by blotting on absorbent paper. Thereafter, 3,3′,5,5′-tetramethylbenzidine (TMB) (GenScript) substrate was added to each well. Colorimetric reaction was stopped by adding 1 M H_2SO_4 and absorbance was measured at 450 nm using a Victor X4 plate reader (Perkin-Elmer). All

ELISA data were normalized for the signal for the highest concentration of βarr2^{+V2Rpp} - Fab30 complex, which was treated as 100%.

Co-immunoprecipitation—Purified βarr2 (5 μg per 100 μL reaction in 20 mM HEPES pH 7.4, 150 mM NaCl buffer) was activated with V_2Rpp or C7pp for 30 min at room temperature (25°C) in tumbling conditions. Subsequently, Fab30 (2.5 μg) was added and allowed for binding at room temperature for 1 h followed by the addition of pre-washed and equilibrated (in 20 mM HEPES pH 7.4 and 150 mM NaCl buffer) Protein-L beads to the reaction mixture and additional tumbling at room temperature for 1 h. Afterwards, beads were washed 4–5 times with 20 mM HEPES pH 7.4, 150 mM NaCl, and 0.01% LMNG buffer, and bound proteins were eluted with 2X SDS loading buffer. Samples were run separately using SDS-PAGE (12% gel) followed by western blotting using HRP-coupled M2 anti-FLAG antibody at 1:5000 dilution.

HDX-MS Analysis—βarr2 protein samples were prepared in 100 μM as a final concentration in 20 mM HEPES pH 7.4 and 150 mM NaCl. For peptide binding, 500 μM of peptide was added to βarr2 and incubated for 1 h at room temperature. Hydrogen/deuterium exchange was initiated by mixing 2 μLof protein samples with 28 μLof D_2O buffer (20 mM HEPES pH 7.4, 150 mM NaCl, and 10% glycerol in D_2O) and incubating for 10, 100, 1000, or 10 000 seconds on ice. At the indicated time points, the reaction was slowed down by the addition of 30 μL of ice-cold quench buffer (100 mM NaH_2PO_4 pH 2.01). For non-deuterated samples, 2 μL of protein sample was mixed with 28 μL of H_2O buffer (20 mM HEPES pH 7.4 and 150 mM NaCl in H_2O) and quenched with 30 μL of ice-cold quench buffer. The quenched samples were digested online by passing through an immobilized pepsin column (2.1 × 30 mm) at a flow rate of 100 mL/min with 0.05% formic acid in H_2O at 12°C. Peptide fragments were subsequently collected on a C18 VanGuard trap column (1.7 mm × 30 mm) for desalting with 0.05% formic acid in H2O. Proteins were then separated by ultra-pressure liquid chromatography over an ACQUITY UPLC C18 column (1.7 mm, 1.0 mm × 100 mm) at a flow rate of 40 mL/min with an acetonitrile gradient created by two pumps, which started with 8% B and increased to 85% B over the next 8.5 min. Mobile phase A was 0.15% formic acid in H_2O and mobile phase B was 0.15% formic acid in acetonitrile. To minimize the back exchange of deuterium to hydrogen, the sample, solvents, trap, and UPLC column were all maintained at a pH of 2.5 and 0.5°C during analysis. Mass spectral analyses were performed with a Xevo G2 QTof equipped with a standard ESI source (Waters, Milford, MA, USA). The mass spectra were acquired in the range of m/z 100–2000 for 12 min in the positive ion mode. Peptides were identified in non-deuterated samples with ProteinLynx Global Server (PLGS) 2.4 (Waters, Milford, MA, USA). The following parameters were applied: monoisotopic mass, non-specific for the enzyme while allowing up to 1 missed cleavage, MS/MS ion searches, automatic fragment mass tolerance, and automatic peptide mass tolerance. Searches were performed with the variable methionine oxidation modification and the peptides were filtered with a peptide score of 6. To process the HDX-MS data, the amount of deuterium in each peptide was determined by measuring the centroid of the isotopic distribution using DynamX 2.0 (Waters, Milford, MA, USA). All measurements were performed with three independent

experiments and statistical significance was analyzed by one-way ANOVA. Back-exchange levels were not corrected because the analyses compared different states.

Confocal Microscopy—To visualize the agonist dependent βarr2 recruitment, HEK-293 cells were transfected with 3.5 μg of CXCR7 construct together with 3.5 μg of βarr2-YFPor βarr2-mCherry mixed with 21 μLof polyethyleneimines (linear). After 24 h of transfection, the cells were trypsinized and seeded at one million density on a 35 × 10 mm confocal dish pretreated with 0.01% poly-D-lysine solution (Sigma). After 48 h of post-transfection, the cells were starved for 4 h in serum-free Dulbecco's Modified Eagle Medium. For live cell imaging, a Zeiss LSM 710 NLO confocal microscope with an oil-immersion 63X/1.40 NA objective, housed inside a CO_2 and temperature-controlled platform was used. A Multi-Line argon laser and diode pump solid state laser at 488 nm and 561 nm was used for imaging YFP-tagged and mCherry-tagged βarr2, respectively, with a 32× array GaAsP descanned detector (Zeiss). ACKR3 agonist VUF11207 (Sigma) at 1 μM was used for stimulation. Image processing was performed using the ZEN-black/ZEN-blue software suite (Zeiss).

Tango Assay—The Tango assay measures β-arrestin recruitment to the receptor. The HTLA cell line, a derivative of the HEK-293 cell line that stably expresses a tTA dependent luciferase reporter gene and β-arrestin2-TEV fusion gene was maintained in Dulbecco's Minimum Essential Media supplemented with 10% fetal bovine serum (FBS), 2 μg mL^{-1} puromycin, and 100 μg mL^{-1} hygromycin B at 37°C in 5% CO_2. The DNA constructs used were CXCR7 wild-type, which contains a full-length receptor followed by a tTA transcription factor with a TEV protease site in between. For transfection, 3×10^6 cells were seeded in a 10 cm plate and transfected with 7 μg receptor construct (CXCR7 wild-type) with 21 μL of linear polyethyleneimine (PEI, mass ratio 1:3). The next day, the transfected cells were trypsinized and 5×10^4 cells/well in 100 μL media were seeded in a 96-well white polystyrene microplate and were allowed to adhere to the wells overnight. Thereafter, cells were stimulated for 7–8 h with varying doses of agonist ranging from 1 pM to 10 μM. The ligand concentrations were prepared in incomplete media devoid of FBS. After incubation with the ligand, the media was aspirated and 100 μL luciferin (0.5 μg mL^{-1} in 1 × Hanks' balanced salt solution buffer) was added to each well and the plate was read for luminescence. Data were normalized for the highest dose of the ligand in the CXCR7 wild-type after basal correction and were analyzed using nonlinear regression with the GraphPad Prism software program.

Quantification and Statistical Analysis

For analysis of the time series data, repeated measures ANOVA (rANOVA) was employed at an α level =.01 and the F statistic calculated; time series as a whole was considered to be significant if the F statistic was greater than 1 at the significance level tested. A t-test was used to determine the significance between individual time points of the series. When time series data did not meet the threshold of significance by rANOVA, an unpaired or paired (Student's) t-test was employed to assess the significance between time points. GraphPad Prism software was used for the statistical analysis. All the statistical details of experiments can be found in Figure legends 1E and 2G.

Acknowledgments

The authors thank the staff at Beamlines 5C and 7A of the Pohang Light Source and BL26B1 beamline of SPring-8 (Japan) for their assistance during the X-ray experiments. This study was supported by a grant from the National Research Foundation of Korea, funded by the Korean Government (2015R1A5A1008958, 2015M3D3A1A01064919, and 2018R1A2B2008142, H.H.L.; NRF-2019R1A5A2027340, K.Y.C.; 2018R1D1A1B07040808, H.-J.Y.). The research program in Dr. Shukla's laboratory was supported by an Intermediate Fellowship of the Wellcome Trust/DBT India Alliance Fellowship (grant number IA/I/14/1/501285) awarded to A.K.S., the Science and Engineering Research Board (EMR/2017/003804), the Innovative Young Biotechnologist Award from the Department of Biotechnology (BT/08/IYBA/2014-3), and the Indian Institute of Technology Kanpur. A.K.S. is an Intermediate Fellow of Welcome Trust/DBT India Alliance, EMBO Young Investigator, and Joy Gill Chair Professor.

References

Bandyopadhyay A, Van Eps N, Eger BT, Rauscher S, Yedidi RS, Moroni T, West GM, Robinson KA, Griffin PR, Mitchell J, et al. A novel polar core and weakly fixed c-tail in squid arrestin provide new insight into interaction with rhodopsin. J Mol Biol. 2018; 430:4102–4118. [PubMed: 30120952]

Barnea G, Strapps W, Herrada G, Berman Y, Ong J, Kloss B, Axel R, Lee KJ. The genetic design of signaling cascades to record receptor activation. Proc Natl Acad Sci USA. 2008; 105:66–69.

Cahill TJ 3rd, Thomsen AR, Tarrasch JT, Plouffe B, Nguyen AH, Yang F, Huang LY, Kahsai AW, Bassoni DL, Gavino BJ, et al. Distinct conformations of GPCR-beta-arrestin complexes mediate desensitization, signaling, and endocytosis. Proc Natl Acad Sci USA. 2017; 114:2562–2567. [PubMed: 28223524]

Celver J, Vishnivetskiy SA, Chavkin C, Gurevich VV. Conservation of the phosphate-sensitive elements in the arrestin family of proteins. J Biol Chem. 2002; 277:9043–9048. [PubMed: 11782458]

Chen Q, Perry NA, Vishnivetskiy SA, Berndt S, Gilbert NC, Zhuo Y, Singh PK, Tholen J, Ohi MD, Gurevich EV, et al. Structural basis of arrestin-3 activation and signaling. Nat Commun. 2017; 8:1427. [PubMed: 29127291]

Chen Q, Iverson TM, Gurevich VV. Structural basis of arrestin-dependent signal transduction. Trends Biochem Sci. 2018; 43:412–423. [PubMed: 29636212]

DeWire SM, Ahn S, Lefkowitz RJ, Shenoy SK. Beta-arrestins and cell signaling. Annu Rev Physiol. 2007; 69:483–510. [PubMed: 17305471]

Emsley P, Cowtan K. Coot: model-building tools for molecular graphics. Acta Crystallogr D Biol Crystallogr. 2004; 60:2126–2132. [PubMed: 15572765]

Ghosh E, Dwivedi H, Baidya M, Srivastava A, Kumari P, Stepniewski T, Kim HR, Lee M-H, van Gastel J, Chaturvedi M, et al. Conformational sensors and domain-swapping reveal structural and functional differences between β-arrestin isoforms. Cell Rep. 2019; 28:3287–3299. [PubMed: 31553900]

Gimenez LE, Kook S, Vishnivetskiy SA, Ahmed MR, Gurevich EV, Gurevich VV. Role of receptor-attached phosphates in binding of visual and non-visual arrestins to G protein-coupled receptors. J Biol Chem. 2012; 287:9028–9040. [PubMed: 22275358]

Granzin J, Wilden U, Choe HW, Labahn J, Krafft B, Buldt G. X-ray crystal structure of arrestin from bovine rod outer segments. Nature. 1998; 391:918–921. [PubMed: 9495348]

Granzin J, Cousin A, Weirauch M, Schlesinger R, Buldt G, Batra-Safferling R. Crystal structure of p44, a constitutively active splice variant of visual arrestin. J Mol Biol. 2012; 416:611–618. [PubMed: 22306737]

Granzin J, Stadler A, Cousin A, Schlesinger R, Batra-Safferling R. Structural evidence for the role of polar core residue Arg175 in arrestin activation. Sci Rep. 2015; 5

Gurevich VV, Gurevich EV. The molecular acrobatics of arrestin activation. Trends Pharmacol Sci. 2004; 25:105–111. [PubMed: 15102497]

Han M, Gurevich VV, Vishnivetskiy SA, Sigler PB, Schubert C. Crystal structure of beta-arrestin at 1.9 Å: possible mechanism of receptor binding and membrane translocation. Structure. 2001; 9:869–880. [PubMed: 11566136]

Hirsch JA, Schubert C, Gurevich VV, Sigler PB. The 2.8 Å crystal structure of visual arrestin: a model for arrestin's regulation. Cell. 1999; 97:257–269. [PubMed: 10219246]

Hoffmann F, Muller W, Schutz D, Penfold ME, Wong YH, Schulz S, Stumm R. Rapid uptake and degradation of CXCL12 depend on CXCR7 carboxyl-terminal serine/threonine residues. J Biol Chem. 2012; 287:28362–28377. [PubMed: 22736769]

Kabsch W. XDS. Acta Crystallogr D Biol Crystallogr. 2010; 66:125–132. [PubMed: 20124692]

Kang DS, Kern RC, Puthenveedu MA, von Zastrow M, Williams JC, Benovic JL. Structure of an arrestin2-clathrin complex reveals a novel clathrin binding domain that modulates receptor trafficking. J Biol Chem. 2009; 284:29860–29872. [PubMed: 19710023]

Kang Y, Zhou XE, Gao X, He Y, Liu W, Ishchenko A, Barty A, White TA, Yefanov O, Han GW, et al. Crystal structure of rhodopsin bound to arrestin by femtosecond X-ray laser. Nature. 2015; 523:561–567. [PubMed: 26200343]

Kim YJ, Hofmann KP, Ernst OP, Scheerer P, Choe HW, Sommer ME. Crystal structure of pre-activated arrestin p44. Nature. 2013; 497:142–146. [PubMed: 23604253]

Konermann L, Pan J, Liu YH. Hydrogen exchange mass spectrometry for studying protein structure and dynamics. Chem Soc Rev. 2011; 40:1224–1234. [PubMed: 21173980]

Kovoor A, Celver J, Abdryashitov RI, Chavkin C, Gurevich VV. Targeted construction of phosphorylation-independent beta-arrestin mutants with constitutive activity in cells. J Biol Chem. 1999; 274:6831–6834. [PubMed: 10066734]

Kroeze WK, Sassano MF, Huang XP, Lansu K, McCorvy JD, Giguere PM, Sciaky N, Roth BL. PRESTO-Tango as an open-source resource for interrogation of the druggable human GPCRome. Nat Struct Mol Biol. 2015; 22:362–369. [PubMed: 25895059]

Kumari P, Srivastava A, Banerjee R, Ghosh E, Gupta P, Ranjan R, Chen X, Gupta B, Gupta C, Jaiman D, et al. Functional competence of a partially engaged GPCR-beta-arrestin complex. Nat Commun. 2016; 7

Laskowski RA, Swindells MB. LigPlot+: multiple ligand-protein interaction diagrams for drug discovery. J Chem Inf Model. 2011; 51:2778–2786. [PubMed: 21919503]

Lefkowitz RJ, Rajagopal K, Whalen EJ. New roles for beta-arrestins in cell signaling: not just for seven-transmembrane receptors. Mol Cell. 2006; 24:643–652. [PubMed: 17157248]

Mayer D, Damberger FF, Samarasimhareddy M, Feldmueller M, Vuckovic Z, Flock T, Bauer B, Mutt E, Zosel F, Allain FHT, et al. Distinct G protein-coupled receptor phosphorylation motifs modulate arrestin affinity and activation and global conformation. Nat Commun. 2019; 10:1261. [PubMed: 30890705]

McCoy AJ, Grosse-Kunstleve RW, Adams PD, Winn MD, Storoni LC, Read RJ. Phaser crystallographic software. J Appl Crystallogr. 2007; 40:658–674. [PubMed: 19461840]

Milano SK, Pace HC, Kim YM, Brenner C, Benovic JL. Scaffolding functions of arrestin-2 revealed by crystal structure and mutagenesis. Biochemistry. 2002; 41:3321–3328. [PubMed: 11876640]

Miskei M, Gregus A, Sharma R, Duro N, Zsolyomi F, Fuxreiter M. Fuzziness enables context dependence of protein interactions. FEBS Lett. 2017; 591:2682–2695. [PubMed: 28762260]

Murshudov GN, Vagin AA, Dodson EJ. Refinement of macro-molecular structures by the maximum-likelihood method. Acta Crystallogr D Biol Crystallogr. 1997; 53:240–255. [PubMed: 15299926]

Nobles KN, Xiao K, Ahn S, Shukla AK, Lam CM, Rajagopal S, Strachan RT, Huang TY, Bressler EA, Hara MR, et al. Distinct phosphorylation sites on the beta(2)-adrenergic receptor establish a barcode that encodes differential functions of beta-arrestin. Sci Signal. 2011; 4:ra51. [PubMed: 21868357]

Oakley RH, Laporte SA, Holt JA, Caron MG, Barak LS. Differential affinities of visual arrestin, beta arrestin1, and beta arrestin2 for G protein-coupled receptors delineate two major classes of receptors. J Biol Chem. 2000; 275:17201–17210. [PubMed: 10748214]

Palczewski K, Buczylko J, Imami NR, McDowell JH, Hargrave PA. Role of the carboxyl-terminal region of arrestin in binding to phosphorylated rhodopsin. J Biol Chem. 1991; 266:15334–15339. [PubMed: 1651326]

Rajagopal S, Kim J, Ahn S, Craig S, Lam CM, Gerard NP, Gerard C, Lefkowitz RJ. Beta-arrestin- but not G protein-mediated signaling by the "decoy" receptor CXCR7. Proc Natl Acad Sci USA. 2010; 107:628–632. [PubMed: 20018651]

Reiter E, Lefkowitz RJ. GRKs and beta-arrestins: roles in receptor silencing, trafficking and signaling. Trends Endocrinol Metab. 2006; 17:159–165. [PubMed: 16595179]

Saaber F, Schutz D, Miess E, Abe P, Desikan S, Ashok Kumar P, Balk S, Huang K, Beaulieu JM, Schulz S, et al. ACKR3 regulation of neuronal migration requires ACKR3 phosphorylation, but not beta-arrestin. Cell Rep. 2019; 26:1473–1488.e9. [PubMed: 30726732]

Scheerer P, Sommer ME. Structural mechanism of arrestin activation. Curr Opin Struct Biol. 2017; 45:160–169. [PubMed: 28600951]

Sensoy O, Moreira IS, Morra G. Understanding the differential selectivity of arrestins toward the phosphorylation state of the receptor. ACS Chem Neurosci. 2016; 7:1212–1224. [PubMed: 27405242]

Sente A, Peer R, Srivastava A, Baidya M, Lesk AM, Balaji S, Shukla AK, Babu MM, Flock T. Molecular mechanism of modulating arrestin conformation by GPCR phosphorylation. Nat Struct Mol Biol. 2018; 25:538–545. [PubMed: 29872229]

Shukla AK, Manglik A, Kruse AC, Xiao K, Reis RI, Tseng WC, Staus DP, Hilger D, Uysal S, Huang LY, et al. Structure of active beta-arrestin-1 bound to a G-protein-coupled receptor phosphopeptide. Nature. 2013; 497:137–141. [PubMed: 23604254]

Shukla AK, Westfield GH, Xiao K, Reis RI, Huang LY, Tripathi-Shukla P, Qian J, Li S, Blanc A, Oleskie AN, et al. Visualization of arrestin recruitment by a G-protein-coupled receptor. Nature. 2014; 512:218–222. [PubMed: 25043026]

Skinner JJ, Lim WK, Bedard S, Black BE, Englander SW. Protein dynamics viewed by hydrogen exchange. Protein Sci. 2012; 21:996–1005. [PubMed: 22544544]

Srivastava A, Gupta B, Gupta C, Shukla AK. Emerging functional divergence of beta-arrestin isoforms in GPCR function. Trends Endocrinol Metab. 2015; 26:628–642. [PubMed: 26471844]

Sutton RB, Vishnivetskiy SA, Robert J, Hanson SM, Raman D, Knox E, Kono M, Navarro J, Gurevich VV. Crystal structure of cone arrestin at 2.3Å: evolution of receptor specificity. J Mol Biol. 2005; 354:1069–1080. [PubMed: 16289201]

Thomsen ARB, Plouffe B, Cahill TJ 3rd, Shukla AK, Tarrasch JT, Dosey AM, Kahsai AW, Strachan RT, Pani B, Mahoney JP, et al. GPCR-G protein-beta-arrestin super-complex mediates sustained G protein signaling. Cell. 2016; 166:907–919. [PubMed: 27499021]

Wales TE, Engen JR. Hydrogen exchange mass spectrometry for the analysis of protein dynamics. Mass Spectrom Rev. 2006; 25:158–170. [PubMed: 16208684]

Wei H, Ahn S, Shenoy SK, Karnik SS, Hunyady L, Luttrell LM, Lefkowitz RJ. Independent beta-arrestin 2 and G protein-mediated pathways for angiotensin II activation of extracellular signal-regulated kinases 1 and 2. Proc Natl Acad Sci USA. 2003; 100:10782–10787. [PubMed: 12949261]

Xiao K, Shenoy SK, Nobles K, Lefkowitz RJ. Activation-dependent conformational changes in {beta}-arrestin 2. J Biol Chem. 2004; 279:55744–55753. [PubMed: 15501822]

Xiao K, McClatchy DB, Shukla AK, Zhao Y, Chen M, Shenoy SK, Yates JR 3rd, Lefkowitz RJ. Functional specialization of beta-arrestin interactions revealed by proteomic analysis. Proc Natl Acad Sci USA. 2007; 104:12011–12016. [PubMed: 17620599]

Yang F, Yu X, Liu C, Qu CX, Gong Z, Liu HD, Li FH, Wang HM, He DF, Yi F, et al. Phospho-selective mechanisms of arrestin conformations and functions revealed by unnatural amino acid incorporation and (19)F-NMR. Nat Commun. 2015; 6:8202. [PubMed: 26347956]

Yin W, Li Z, Jin M, Yin Y-L, de Waal PW, Pal K, Yin Y, Gao X, He Y, Gao J, et al. A complex structure of arrestin-2 bound to a G protein-coupled receptor. Cell Res. 2019; 29:971–983. [PubMed: 31776446]

Zhan X, Gimenez LE, Gurevich VV, Spiller BW. Crystal structure of arrestin-3 reveals the basis of the difference in receptor binding between two non-visual subtypes. J Mol Biol. 2011; 406:467–478. [PubMed: 21215759]

Zhou XE, He Y, de Waal PW, Gao X, Kang Y, Van Eps N, Yin Y, Pal K, Goswami D, White TA, et al. Identification of phosphorylation codes for arrestin recruitment by G protein-coupled receptors. Cell. 2017; 170:457–469. [PubMed: 28753425]

Zimmerman B, Simaan M, Akoume MY, Houri N, Chevallier S, Seguela P, Laporte SA. Role of βarrestins in bradykinin B2 receptor-mediated signalling. Cell Signal. 2011; 23:648–659. [PubMed: 21145390]

Europe PMC Funders Author Manuscripts

Europe PMC Funders Author Manuscripts

Highlight

- The structure of β-arrestin 2 bound to CXCR7 phosphopeptide (C7pp) was solved
- The C7pp-bound β-arrestin 2 shows small inter-domain rotation
- The three C7pp phosphates bind with the positively charged residues on β-arrestin 2
- The phosphate-binding pocket around Arg148 recognizes the first phosphate of C7pp

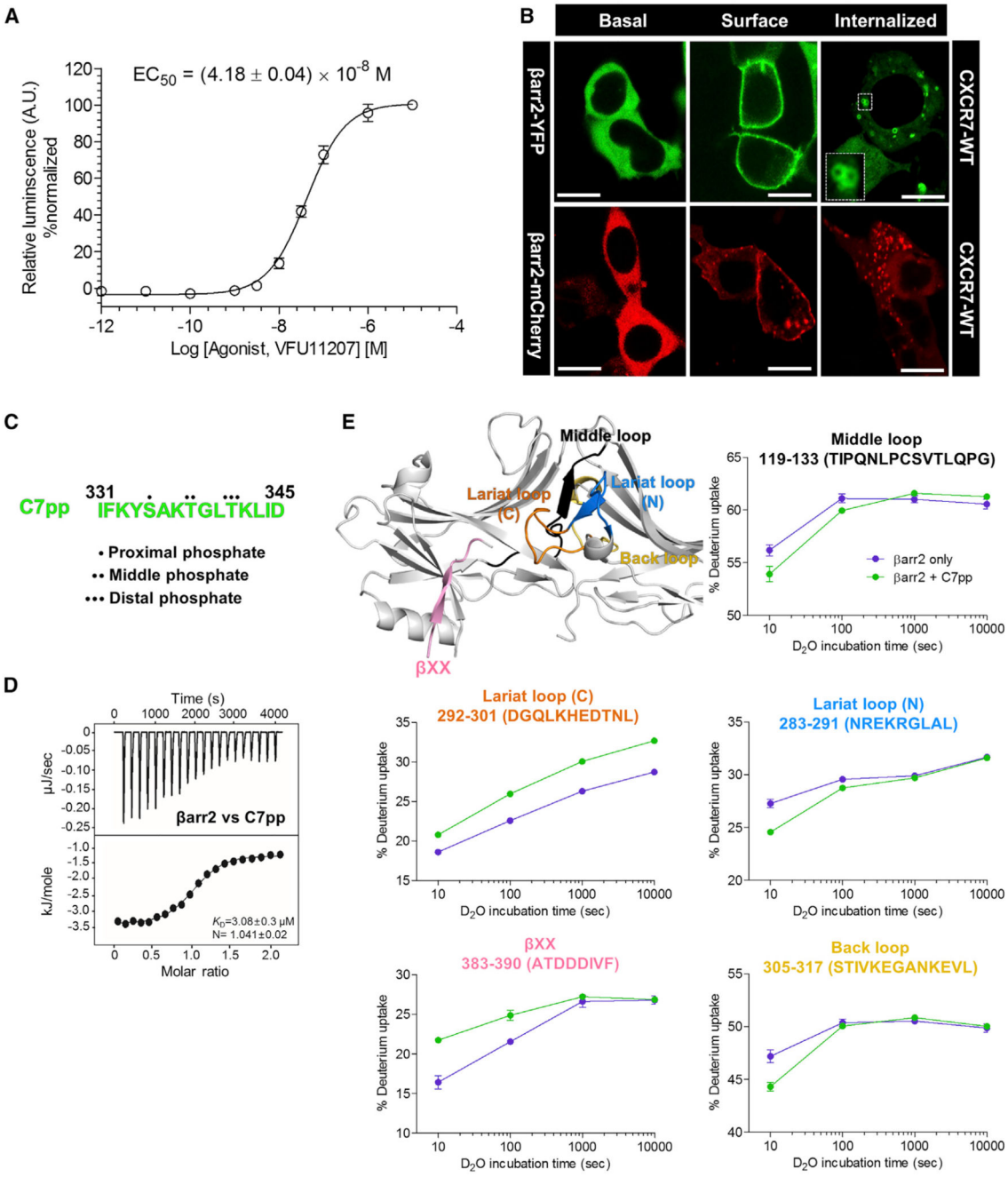

Figure 1. Agonist-Induced βarr2 Recruitment and Trafficking for the Human CXCR7 and HDX-MS Profile of CXCR7 Phosphopeptides with βarr2

(A) Agonist-induced recruitment of βarr2 for CXCR7 measured using the PRESTO-TANGO assay. HTLA cells expressing N-terminal FLAG-tagged CXCR7 were stimulated with an indicated concentration of agonist (VUF11207), followed by measurement of the luminescence output as a readout of βarr2 recruitment. The data from three independent experiments, each performed in duplicate, were normalized for maximal response (treated as 100%). Data represent the mean ± standard error of the mean of three independent experiments.

Europe PMC Funders Author Manuscripts

(B) Agonist-induced βarr2 trafficking was monitored with confocal microscopy. HEK-293 cells expressing CXCR7 together with either βarr2-YFP or βarr2-mCherry were stimulated with a saturating concentration of agonist, followed by live cell imaging using the corresponding wavelengths. Representative images from three independent experiments are presented to indicate agonist-induced surface translocation of βarr2 followed by endosomal trafficking. Scale bars represent μ0 mm.

(C) Peptide sequence of the CXCR7 phosphopeptide referred to as C7pp hereafter, colored in green. The positions of the proximal, middle, and distal phosphates are denoted by dots. See also Figure S1A.

(D) Binding affinity of CXCR7 phosphopeptide with βarr2 measured with isothermal calorimetry. Purified βarr2 was incubated with increasing C7pp concentrations, and the binding parameters were calculated based on the dose-response curve. The binding constant for the peptide and stoichiometry as observed in three independent experiments (n = 3) is presented.

(E) HDX-MS profile of βarr2 upon C7pp binding. Regions with altered HDX profile are color coded on the inactive structure of βarr2 (PDB: 3P2D), and the deuterium uptake plots of color-coded regions are provided. Data represent the mean ± standard error of the mean of three independent experiments. Statistical analysis was performed using one-way analysis of variance (ANOVA) followed by Tukey's post test (*$p < 0.05$ compared with βarr2 alone). Differences smaller than 0.3 Da were not considered significant. See also Figure S1B.

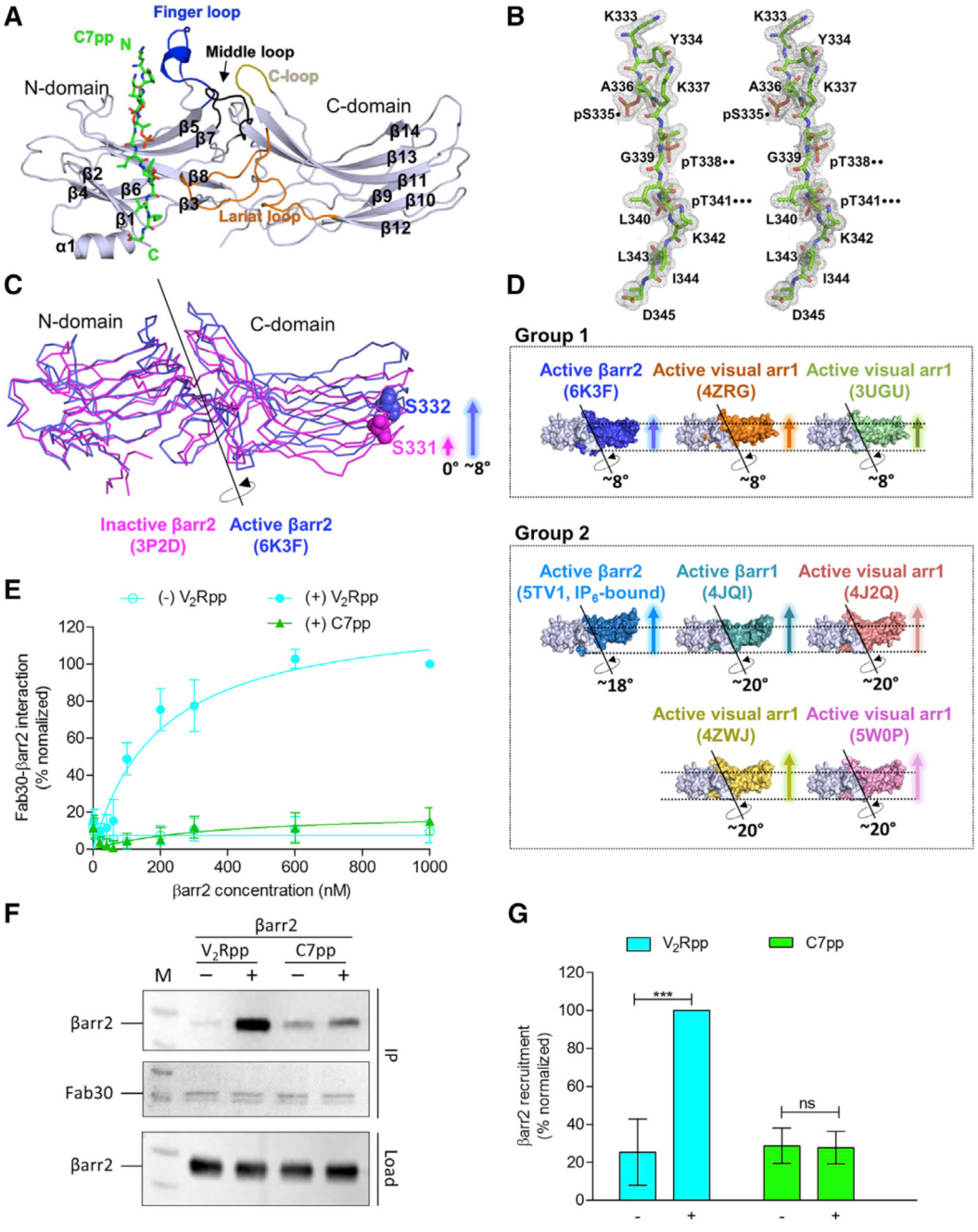

Figure 2. C7pp-Bound βarr2 Exhibits a Smaller Inter-domain Rotation Compared with V_2Rpp-βarr1, and the Fab30 Sensor Corroborates the Observation

(A) Overall structural snapshot of C7pp-bound βarr2 highlighting the loop regions. The C7pp peptide is shown as green sticks and the various loops in βarr2, i.e., the finger, middle, lariat, and C loops in the central crest, are colored in blue, black, orange, and olive, respectively. See also Figure S2.

(B) The stereo $2F_o$-F_c map for C7pp is drawn with a 1.0σ contour. The positions of the proximal, middle, and distal phosphates of the phospho-cluster (PxxPxxP) are denoted by dots.

(C) The inter-domain rotation angle of βarr2 in complex with C7pp. The N domains of active and inactive βarr2 structures are superimposed, and the rotation axis is shown. The relative positions of Ser^{332} of the active βarr2 (PDB: 6K3F) are shown in ball representation as a reference for comparison. The crystal structure of βarr2 in complex with C7pp (blue) reveals an inter-domain rotation of approximately 8° compared with the inactive βarr2 structure (PDB: 3P2D, magenta).

(D) Various inter-domain rotation angles of arrestins are shown, based on previous references (PDB: 4ZRG, visual arr1 R175E; 3UGU, visual arr1 p44; 5TV1, IP_6-bound βarr2; 4JQI, V_2Rpp-bound βarr1; 4J2Q, visual arr1 p44; 4ZWJ, rhodopsin-bound visual arr1; 5W0P, rhodopsin-bound visual arr1) (Chen et al., 2017; Granzin et al., 2012, 2015; Kang et al., 2015; Kim et al., 2013; Shukla et al., 2013; Zhou et al., 2017). See also Figure S4.

(E) The Fab30 reactivity pattern corroborates the structural differences between V_2Rpp-bound βarr2 and C7pp-bound βarr2. Increasing concentrations of βarr2 in the presence of a saturating concentration of different phosphopeptides were immobilized on an ELISA plate followed by incubation with Fab30 and detection using HRP-coupled Protein-L. Data were normalized with the maximal response for V_2Rpp-βarr2 condition (treated as 100%). Data represent the mean ± standard error of the mean of three independent experiments.

(F) Co-immunoprecipitation experiments further confirm the Fab30 reactivity patterns as observed in the ELISA. Purified βarr2 was incubated with a saturating concentration of different phosphopeptides followed by the addition of 1.5-fold molar excess of Fab30. Thereafter, Fab30 was immunoprecipitated using Protein-L agarose and the interaction of Fab30 and βarr2 was visualized using western blotting. A representative image from three independent experiments is shown here.

(G) Densitometry-based quantification of data presented in (F) normalized for maximal response to the V_2Rpp-βarr2 condition (treated as 100%). Data were analyzed using one-way ANOVA with the Bonferroni post test (***$p < 0.001$; ns, not significant).

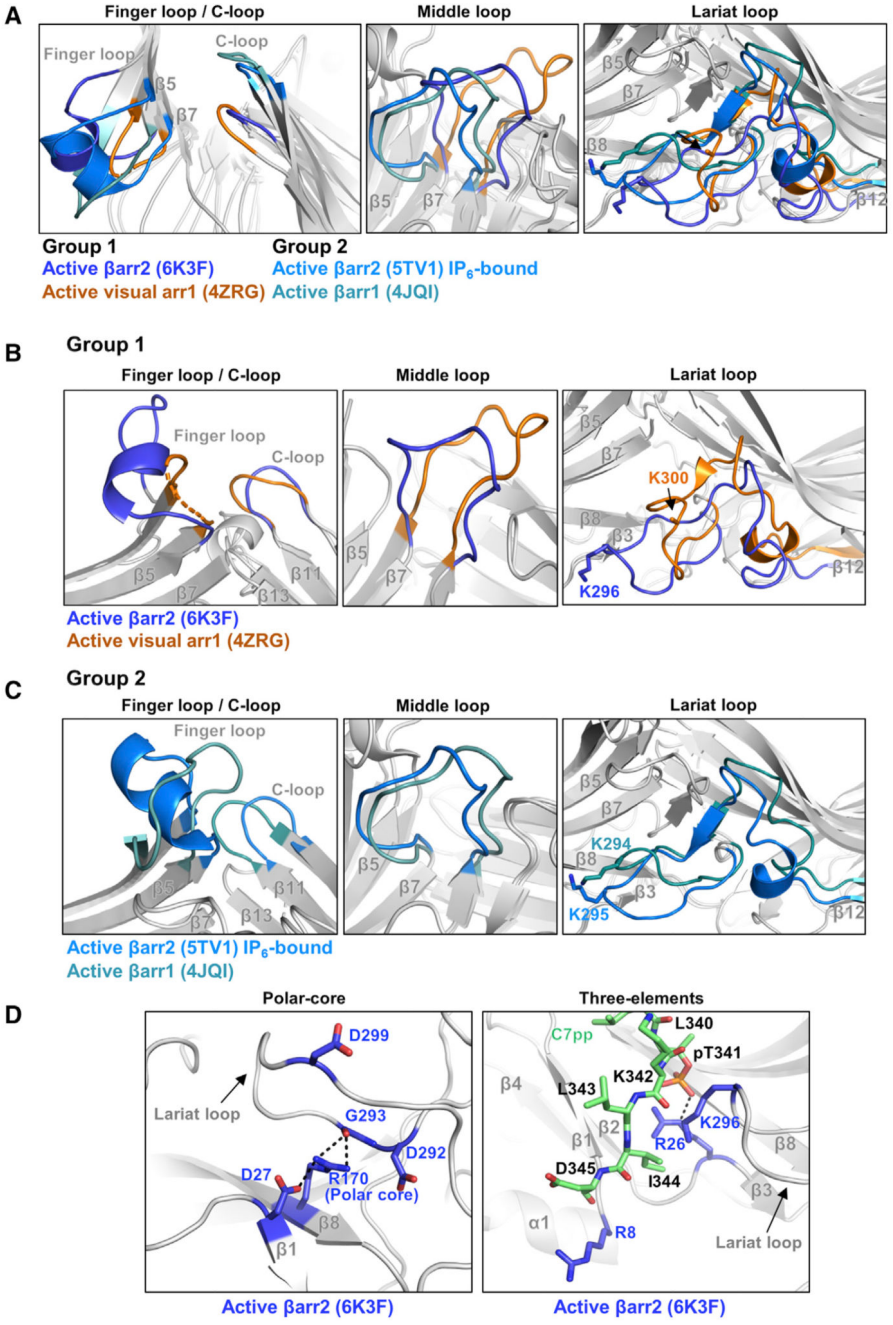

Figure 3. Conformational Changes in Various Loops of βarr2 upon C7pp Binding as Observed in the Crystal Structure

(A) Structural comparisons of the finger, middle, lariat, and C loops in C7pp-bound βarr2 (PDB: 6K3F, blue), R175E visual arr1 (PDB: 4ZRG, orange), IP_6-bound βarr2 (PDB: 5TV1, light blue), and V_2Rpp-bound βarr1 (PDB: 4JQI, light cyan).

(B) Structural comparisons of the finger, middle, lariat, and C loops in C7pp-bound βarr2 (PDB: 6K3F, blue) and R175E visual arr1 (PDB: 4ZRG, orange).

(C) Structural comparisons of the finger, middle, lariat, and C loops in IP_6-bound βarr2 (PDB: 5TV1, light blue) and V_2Rpp-bound βarr1 (PDB: 4JQI, light cyan).

(D) Structural comparisons of polar-core and 3E interactions in C7pp-bound βarr2 (PDB: 6K3F, blue). The C7pp is colored green.
See also Figure S5.

Europe PMC Funders Author Manuscripts

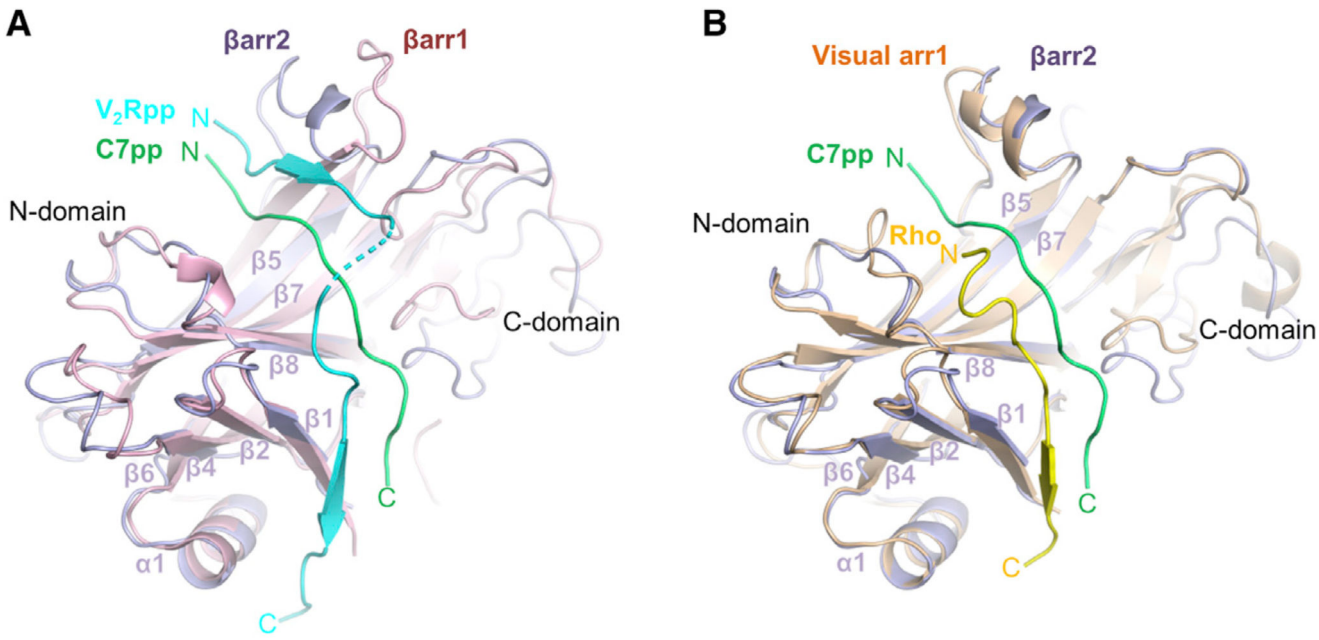

Figure 4. An Overall Distinct Binding Mode of C7pp with βarr2

(A) An overall distinct binding mode of C7pp with βarr2 (PDB: 6K3F, green) compared with the V_2Rpp-βarr1 complex (PDB: 4JQI, light cyan). The N domains from the crystal structures of the C7pp-βarr2 complex and V_2Rpp-βarr1 are superimposed and the respective phosphopeptides are highlighted for comparison.

(B) Comparison of binding modes of C7pp with βarr2 (PDB: 6K3F, green) and the rhodopsin R_p-tail with visual arr1 (PDB: 5W0P, yellow), similar to that shown in (A). See also Figure S3.

Europe PMC Funders Author Manuscripts

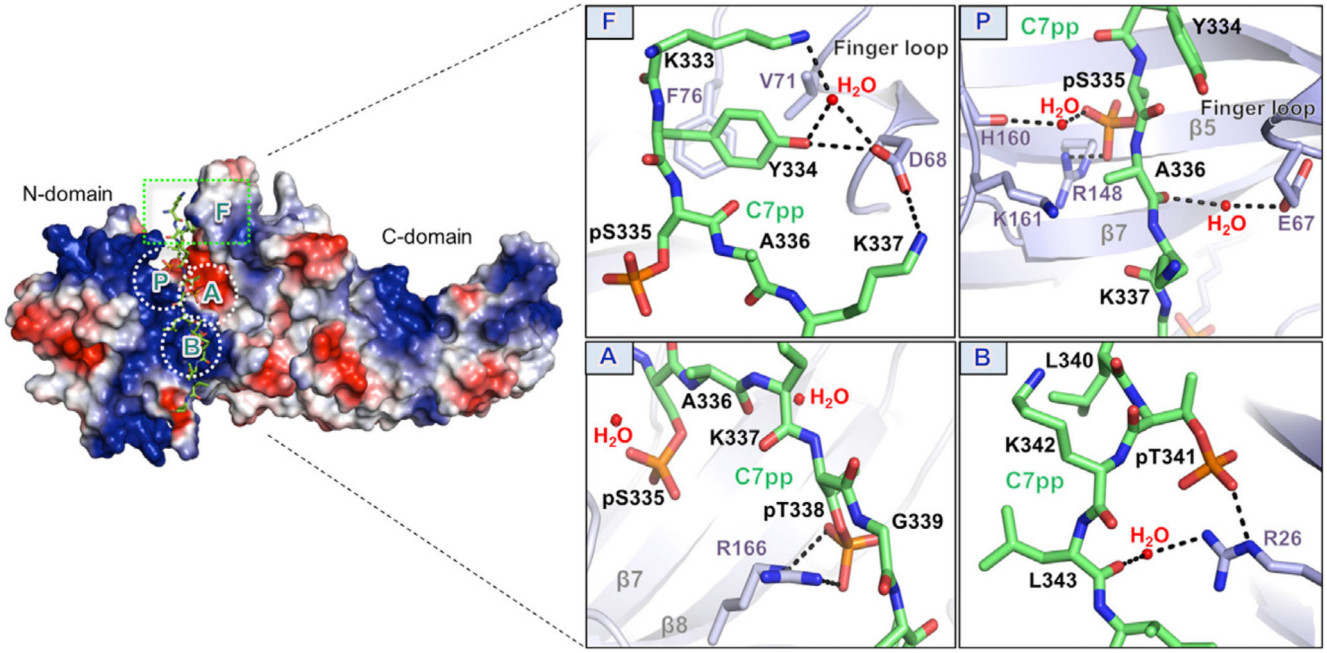

Figure 5. Overall Binding Mode of C7pp to βarr2 with Specific Interactions of the Phosphate Groups and Activation Switches

Surface representation of the overall electrostatic potential of the C7pp-bound βarr2 structure. C7pp is shown as green sticks. In the positive electrostatic surface of the N domain, the four hotspots for C7pp binding are shown in the dotted rectangle or circles (F, P, A, and B). The panels on the right represent the detailed interactions at the βarr2-C7pp interface and specific interactions of the phosphates with various residues in βarr2. See also Figures S1B and S6.

Europe PMC Funders Author Manuscripts

Table 1
Statistics for Data Collection and Refinement

Dataset	βarr2 with C7pp
Data Collection Statistics	
X-ray source	SPring-8 26B
X-ray wavelength (Å)	0.97928
Space group	$C2_1$
a, b, c (Å)	91.17, 127.91, 206.04
Resolution range (Å)	50–1.95
Total/unique reflections	538,906/332,324
Completeness (%)	98.1 (96.3)[a]
Average $I/\sigma(I)$	70.7 (2.5)[a]
R_{merge} [b] (%)	39.0 (150.9)[a]
Model Refinement Statistics	
Resolution range (Å)	50–2.3
R_{work}/R_{free} [c] (%)	24.6/28.3
Number/average *B* factor (Å^2)	
Protein nonhydrogen atoms	16,176/32.61
Water oxygen atoms	524/16.82
Peptide nonhydrogen atoms	570/52.28
RMSDs from ideal geometry	
Bond lengths (Å)	0.004
Bond angles (°)	0.878
Protein-geometry analysis (%)	
Ramachandran favored	83.3 (1730/2077)
Ramachandran allowed	14.3 (297/2077)
Ramachandran outliers	2.4 (50/2077)

[a] Values in parentheses refer to the highest-resolution shell (1.95–1.98 Å).

[b] $R_{merge} = \sum hkl \sum i |I_i(hkl) - \langle I(hkl) \rangle| / \sum hkl \sum_i I_i(hkl)$, where $I(hkl)$ is the intensity of reflection hkl, $\sum hkl$ is the sum over all reflections, and $\sum_i$ is the sum over i measurements of reflection hkl.

[c] $R = \sum hkl ||F_{obs}| - |F_{calc}|| / \sum hkl |F_{obs}|$, where R_{free} was calculated for a randomly chosen 5% of reflections, which were not used for structure refinement, and R_{work} was calculated for the remaining reflections.